ACS APPLIED MATERIALS & INTERFACES
Research Article
www.acsami.org

Hierarchical Top-Porous/Bottom-Tubular TiO_2 Nanostructures Decorated with Pd Nanoparticles for Efficient Photoelectrocatalytic Decomposition of Synergistic Pollutants

Zhonghai Zhang, Yanjie Yu, and Peng Wang*

Water Desalination and Reuse Center, Chemical and Life Science and Engineering Division, King Abdullah University of Science and Technology, Thuwal 23955-6900, Kingdom of Saudi Arabia

Supporting Information

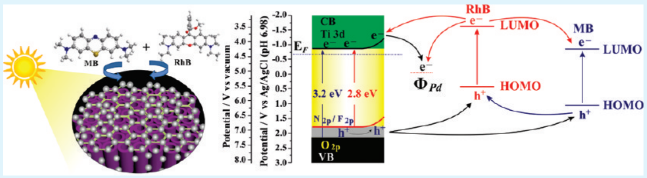

ABSTRACT: In this paper, top-porous and bottom-tubular TiO_2 nanotubes (TiO_2 NTs) loaded with palladium nanoparticles (Pd/TiO_2 NTs) were fabricated as an electrode for an enhanced photoelectrocatalytic (PEC) activity toward organic dye decomposition. TiO_2 NTs with a unique hierarchical top-porous and bottom-tubular structure were prepared by a facile two-step anodization method and Pd nanoparticles were decorated onto the TiO_2 NTs via a photoreduction process. The PEC activity of Pd/TiO_2 NTs was investigated by decomposition of methylene blue (MB) and Rhodamine B (RhB). Because of formation Schottky junctions between TiO_2 and Pd, which significantly promoted the electron transfer and reduced the recombination of photogenerated electrons and holes, the Pd/TiO_2 NT electrode showed significantly higher PEC activities than TiO_2 NTs. Interestingly, an obvious synergy between two dyes was observed and corresponding mechanism based on facilitated transfer of electrons and holes as a result of a suitable energy level alignment was suggested. The findings of this work provide a fundamental insight not only into the fabrication but also utility of Schottky junctions for enhanced environmental remediation processes.

KEYWORDS: *TiO_2 nanotube, Schottky junction, Pd nanoparticles, photoelectrocatalysis*

1. INTRODUCTION

TiO_2 has been widely utilized as an effective photocatalytic (PC) material because of its chemical and optical stability, nontoxicity and low cost.[1] TiO_2 nanotubes arrays (TiO_2 NTs), fabricated by anodization process, have been regarded as one of the most promising materials for PC applications because of their unique electronic properties, especially their high electron mobility induced by their one-dimensional nanostructure, and therefore are being intensively studied in pollutants decomposition,[2−5] water splitting,[6−10] and solar cells.[11−14] The two-step anodization is a rational alternative to the conventional TiO_2 NT anodization method, which suffers from disparity in tube lengths and considerable tube array surface roughness. Furthermore, under suitable synthesis conditions, the two-step anodization method can facilely fabricate unique hierarchical top-porous/bottom-tubular TiO_2 NTs, which have been proven to perform better in water splitting and in sensitized solar cells than the conventional TiO_2 NTs.[15−17]

Metal nanoparticle decoration is an effective way to enhance the PC activity of TiO_2 NTs. In this paper, Pd nanoparticles were decorated on TiO_2 NTs by a facile photoreduction method. As the electron affinity of anatase TiO_2 (~4.2 eV)[18] is significantly lower than the work function of Pd (~5.12 eV),[19] a potential barrier (i.e., Schottky potential barrier) exists at the interfaces between TiO_2 NTs and Pd nanoparticles, which makes the electron transfer from the TiO_2 conduction band to Pd energetically favorable. Pd was chosen due to its suitable work function and a relatively low cost (731 USD/oz). The high Φ_{Pd} of Pd favors the electron transfer and reduction of the electron−hole recombination, and its low price allows for its large-scale production and applications. Pt (Φ_{Pt} = 5.65 eV)[19] and Au (Φ_{Au} = 5.10 eV)[20] also own suitable work functions, but their high prices (>1700 USD/oz) severely limit their large-scale applications.

In this study, the Pd decorated top-porous/bottom-tubular TiO_2 NTs (Pd/TiO_2 NTs) were fabricated, and their PC and photoelectrocatalytic (PEC) activities were determined by decomposition of single and mixed dyes (i.e., methylene blue (MB) and Rhodamine B (RhB)). Although the Pd has been deposited on conventional TiO_2 NTs for adsorption[21,22] or photocatalysis study,[23] to the best of our knowledge, there are no reports on noble metal nanoparticles decoration of hierarchical TiO_2 NTs and interestingly enough, an obviously synergistic effect between MB and RhB was first observed and corresponding mechanism was suggested.

2. EXPERIMENTAL SECTION

2.1. Chemicals and Materials. A 2 mm thick titanium sheet (99.6%, Strem Chemicals) was cut into pieces of 25 × 10 mm^2. Palladium(II) acetylacetonate ($Pd(AcAc)_2$, Sigma-Aldrich Chemicals, 99%) was used as the precursor of Pd nanoparticles. Ethylene glycol

Received: November 21, 2011
Accepted: January 10, 2012
Published: January 10, 2012

dx.doi.org/10.1021/am201630s | *ACS Appl. Mater. Interfaces* 2012, 4, 990−996

(EG), ammonia fluoride (NH_4F), Rhodamine B (RhB), methylene blue (MB), and sodium sulfate (Na_2SO_4) were purchased from Acros Organics and used as received. All aqueous solutions were prepared using deionized water with a resistivity of 18.2 MΩ cm prepared by Millipore system.

2.2. Preparation of Top-Porous TiO_2 Nanotube Arrays Electrode. The top-porous and bottom-tubular TiO_2 NTs were fabricated by a two-step anodization process. Prior to anodization, the Ti sheets were first degreased by sonicating in ethanol and cold distilled water, followed by drying in pure nitrogen stream. The anodization was carried out using a conventional two-electrode system with the Ti sheet as an anode and a Pt gauze (Aldrich, 100 mesh) as a cathode respectively. All electrolytes consisted of 0.5 wt % NH_4F in EG solution with 2 vol% water. All the anodization was carried out at room temperature. In the first-step anodization, the Ti sheet was anodized at 50 V for 10 min, then the as-grown nanotube layer was ultrasonically removed in deionized water. The same Ti sheet then underwent the second anodization at 50 V for 30 min. After the two-step anodization, the prepared TiO_2 NT sample was cleaned with distilled water and dried off with N_2 gas. The as-anodized TiO_2 NTs were annealed in air at 450 °C for 1 h with a heating rate of 5 °C/min.

2.3. Decoration of Pd on TiO_2 NTs. Pd nanoparticles were decorated on the previously prepared TiO_2 NTs by a photocatalytic reduction method using $Pd(AcAc)_2$ as a precursor. $Pd(AcAc)_2$ was diluted in deionized water and ethanol with a water/ethanol volume ratio of 10:1, and the concentration of $Pd(AcAc)_2$ was fixed at 1 mM. The Ti sheet containing the prepared TiO_2 NTs were soaked into the palladium precursor solution for 24 h, rinsed with deionized water, and subsequently irradiated with simulated solar light for 30 min.

2.4. Characterization of Pd/TiO_2 NTs. The morphology of nanotubular structures and distribution of nanoparticles were determined by filed-emission scanning electron microscope (FESEM, FEI Quanta 600) and transmission electron microscope (TEM, Tecnai T12). The chemical compositions of Pd/TiO_2 NTs were analyzed by energy dispersive spectrometer (EDS) equipped with FESEM. The crystalline structure was analyzed by X-ray diffraction (XRD, Bruker D8 Discover diffractometer, using Cu Kα radiation, λ = 1.540598 Å). X-ray Photoelectron Spectroscopy (XPS) data were collected by an Axis Ultra instrument (Kratos Analytical) under ultrahigh vacuum ($<1 \times 10^{-8}$ Torr) and by using a monochromatic Al Kα X-ray source operating at 150 W. The survey and high-resolution spectra were collected at fixed analyzer pass energies of 160 and 20 eV, respectively. Binding energies were referenced to the C 1s binding energy of adventitious carbon contamination which was taken to be 285.0 eV.

2.5. Photoelectrochemical Characterization of Pd/TiO_2 NTs. The photoelectrochemical performance of the Pd/TiO_2 NTs was evaluated using a three-electrode configuration with Pd/TiO_2 NT electrode, Ag/AgCl electrode, and Pt mesh as working, reference, and counter electrode, respectively. The supporting electrolyte used was 50 mM Na_2SO_4 solution. All the potentials were referred to Ag/AgCl electrode unless otherwise stated in this paper. The photocurrent was measured under an irradiation from a 300 W Xe lamp (PLS-SXE300, PE300BF). The intensity of light source was calibrated with a Si diode (Newport) to simulate AM 1.5 illumination (100 mW cm^{-2}). The scan rate for the linear sweep voltammetry was 5 mV s^{-1}. The photoresponse was evaluated under chopped light irradiation (light on/off cycles: 60 s) at a fixed electrode potential of 0.5 V. The electrochemical impedance spectra (EIS) were performed using a PGSTAT302N Autolab Potentiostat/Galvanostat (Metrohm) equipped with a frequency analyzer module (FRA2) with an excitation signal of 10 mV amplitude. The impedance vs frequency spectra were acquired at open circular potential under illumination condition. Afterward, impedance vs potential measurement at fixed frequencies was performed for determined the flat-band potential and carrier density.

2.6. Photoelectrocatalytic Decomposition of Mixed Dyes on Pd/TiO_2 NTs. PEC degradation experiments were carried out in a pyrex reactor with Pd/TiO_2 NTs as photoelectrode, and the active area was 1.0 cm^2 under illumination of the same light source as the photoelectrochemical characterization experiments. Mixed dye solution with RhB (2.5 mg L^{-1}) and MB (4.0 mg L^{-1}) was used; 50 mM Na_2SO_4 was used as the supporting electrolyte in call cases. The solution was stirred continuously during the whole PC and PEC processes. The decomposition of the dyes was monitored with UV−vis absorption spectra at 10 min interval with characteristic absorbance at 552 and 662 nm for RhB and MB, respectively. The RhB (2.5 mg L^{-1}) and MB (4.0 mg L^{-1}) solution were also separately decomposed on TiO_2 NTs and Pd/TiO_2 NTs for comparison.

3. RESULTS AND DISCUSSION

Scheme 1 presents a schematic diagram of the fabrication procedure of Pd/TiO_2 NTs. Briefly, first, a pristine Ti sheet was anodized and the as-grown TiO_2 NTs were removed by ultrasonication, leaving behind ordered hexagonal imprints on the surface of the Ti sheet; second, the Ti sheet with these imprints was anodized again, during which the hexagonal imprints formed top-porous structure and individual NTs were grown below the top-porous layer. The as-anodized TiO_2 NTs were annealed in air at 450 °C for 1 h with a heating rate of 5 °C/min for crystallization to have pure anatase formed (see Figure S1 in the Supporting Information). Pd nanoparticles were then deposited onto the top-porous structures and into the bottom-tubular TiO_2 NTs by a photoreduction method.

Scheme 1. Scheme of the Fabrication Procedure of Pd/TiO_2 NTs

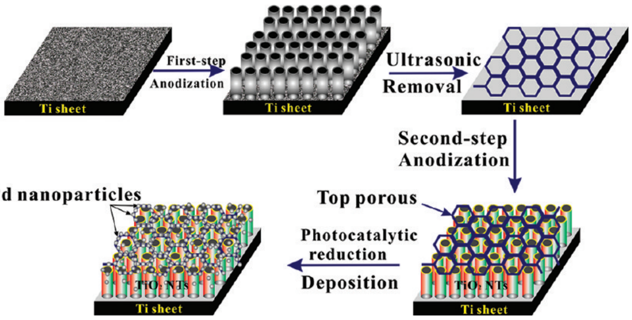

Figure 1a presents a top view SEM image of the as-prepared TiO_2 NTs. A unique top hexagonally porous structure is clearly observed, with an average diameter of the hexagonal pores at ~200 nm and a wall-thickness of ~25 nm. With the top porous structure removed, the bottom nanotube arrays are visible in top-right inset of Figure 1a, with an average inner diameter of ~60 nm and a wall thickness of ~20 nm. A cross-sectional view of the TiO_2 NTs is presented in the bottom-left inset of Figure 1a, which indicates a uniform tubular structure with a length of about 2 μm. The top-view SEM image of Pd/TiO_2 NTs clearly shows that there is no big Pd nanoparticle aggregates visible (Figure 1b). Figure 1c is a high-magnification top-view SEM image of Pd/TiO_2 NTs, which shows the Pd nanoparticles with an average size of 20 nm are uniformly decorated on the top porous TiO_2 structure and also inside the tubes. Figure 1d shows a cross-sectional SEM image of Pd/TiO_2 NTs, indicating that Pd nanoparticles are uniformly decorated also on the outer wall surfaces of the vertically aligned NTs, in line with the SEM image in Figure 1e. Figure 1f is a TEM image of Pd/TiO_2 NTs, which further confirms the presence of Pd inside the tubes. The elemental analysis results from EDS (Figure S2 in the Supporting Information) confirm a uniform distribution of Pd on the TiO_2 NT surface and show the significant existence

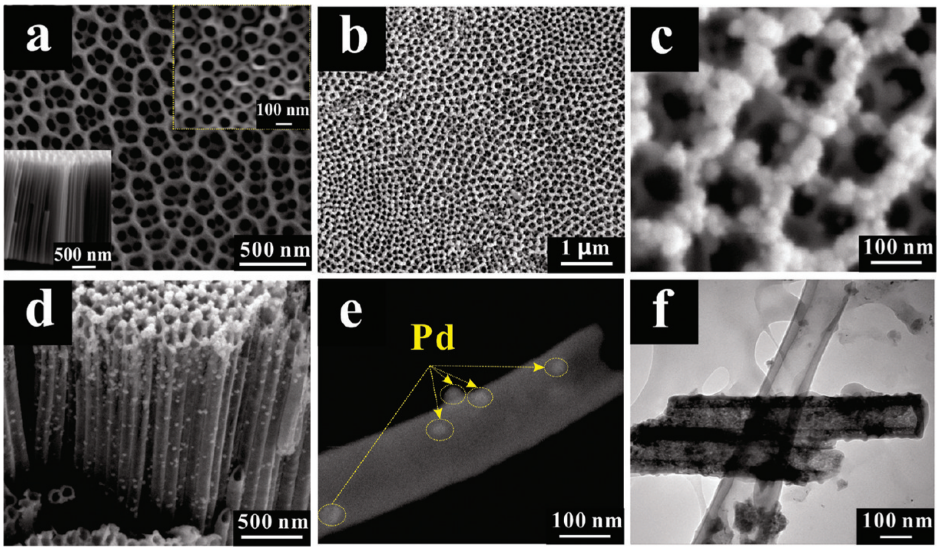

Figure 1. (a) SEM top-view image of top-porous and bottom-tubular TiO_2 NTs, the top right inset shows the TiO_2 NTs with the top-porous structure removed, and the bottom left inset shows a cross-sectional view of TiO_2 NTs; (b) SEM top-view image of Pd/TiO_2 NTs; (c) high-magnification of Pd nanoparticles associated with Pd/TiO_2 NTs ; (d) cross-sectional SEM image of Pd/TiO_2 NTs; (e) SEM image of single TiO_2 NT with Pd nanoparticles on its outer surface; and (f) TEM image of TiO_2 NTs with Pd nanoparticles inside the tubes.

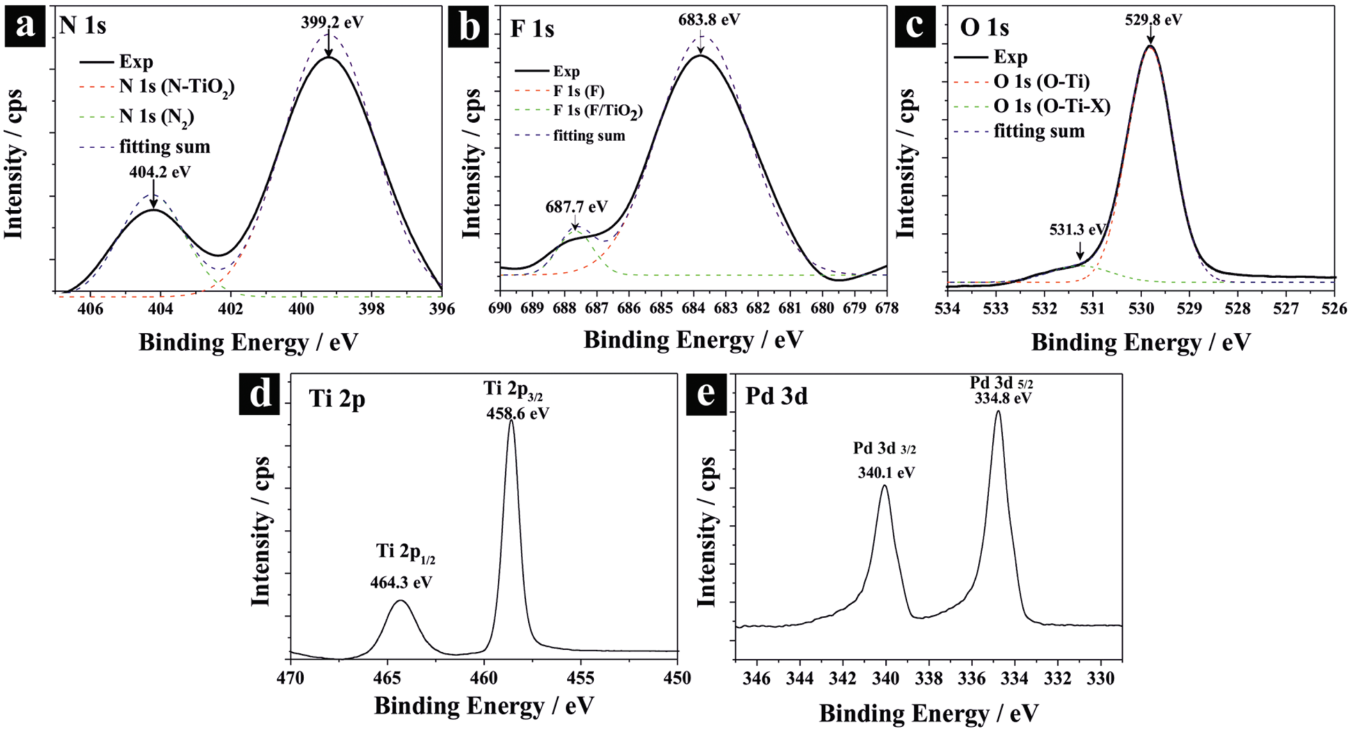

Figure 2. Core-level XPS of (a) N 1s, (b) F 1s, (c) O 1s, (d) Ti 2p, and (e) Pd 3d.

of N and F, which is ascribed to inherent titanium's interaction with NH_4F electrolyte during the anodization process.

XPS analysis was conducted to determine the valence state of Pd, and the status of N and F in Pd/TiO_2 NTs. As shown in Figure 2, a dominant signal with its peak at 399.2 eV appears in the N 1s region, which implies almost all the N was doped into the TiO_2 lattice. The weak peak at 404.2 eV may be ascribed to the chemical adsorption of N_2. As N−Ti−N structure is formed in the TiO_2, a relatively low binding energy around 396 eV is generally detected. On the other hand, the formation of O−Ti−N structure by partially substituting O atoms for N atoms can lead to a higher binding energy of N 1s because of a lower electronegativity of N than O, which corresponds to the state of the doped nitrogen with a binding energy of around 400 eV.[24] Thus, we believe that the state of the nitrogen doped in our case is the latter case, namely, the formation of N−Ti−O structure. The core-level XPS spectrum of F 1s is presented in Figure 2b. Unlike N, most of the F existed in its molecular form as indicated with a strong XPS peak at 683.8 eV. The moderate peak at 687.7 eV indicates a small portion of F was substituted into the TiO_2 lattice.[25] The nonmetal, such as N, F, doping would modify the band edge structure of TiO_2 and thus expand

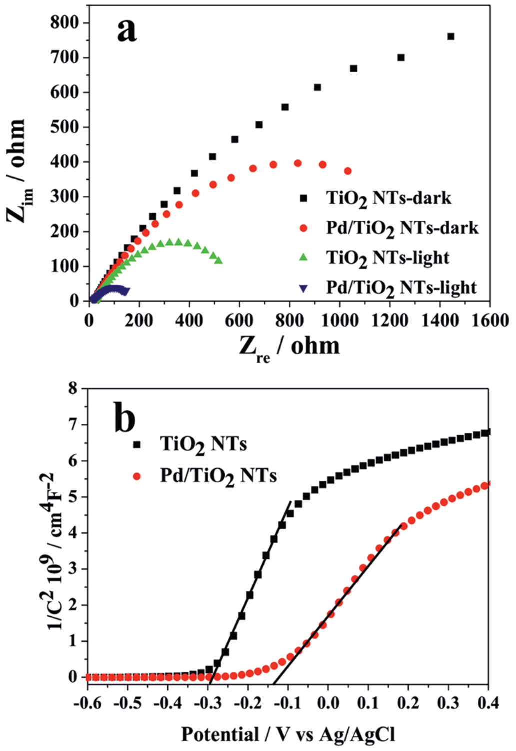

Figure 3. (a) Electrochemical impedance spectra of Nyquist plots (Z_{re} vs Z_{im}), and (b) Mott−Schottky plot at a fixed frequency of 5k Hz on TiO_2 NTs and Pd/TiO_2.

its optical absorption into visible light region, which is advantageous to practical applications where solar light is the main energy source. The core-level XPS of O 1s in Figure 2c shows a two-band structure. A dominant peak at 529.8 eV is characteristic of metal oxides, which is in agreement with O 1s electron binding energy for TiO_2, whereas an additional peak at 531.3 eV implies the formation of impure band structures, such as N−Ti−O or F−Ti−O structures.[26] The high-magnification core-level XPS spectra of Ti 2p in Figure 2d shows doublet peaks at 458.6 and 464.3 eV, corresponding to the Ti $2p_{3/2}$ and Ti $2p_{1/2}$, respectively.[27] The XPS Pd 3d spectrum in Figure 2e shows doublet peak at 334.8 and 340.1 eV for Pd $3d_{5/2}$ and Pd $3d_{3/2}$, respectively. The distance between Pd $3d_{3/2}$ and $3d_{5/2}$ being 5.3 eV and the intensity ratio of Pd $3d_{5/2}$ to Pd $3d_{3/2}$ being 3/2, which are expected from theoretical calculations, confirm metallic Pd^0 is the only palladium phase present. The oxidation of Pd would have resulted in a Pd 3d binding energy shift of greater than 1.0 eV and the formation of a Pd alloy containing Ti, for example, Pd_3Ti, would have led to a binding energy shift of 0.5 eV, both of which were not detected.[28,29]

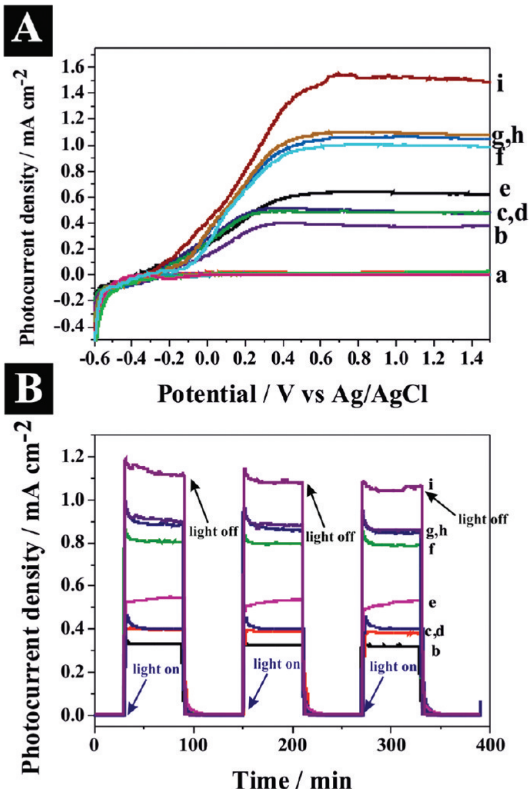

Figure 4. (A) Linear-sweep voltammagrams of TiO_2 NT and Pd/TiO_2 NT electrodes with or without dyes in dark and under illumination. Scan rate is 5 mV/s and supporting electrolyte is 50 mM Na_2SO_4. (B) Corresponding amperometric *I*−*t* curves at an applied potential of 0.5 V vs Ag/AgCl under illumination with 60 s light on/off cycles with or without dyes. (a) in dark; (b) TiO_2 NTs in Na_2SO_4, (c) TiO_2 NTs in Na_2SO_4+MB, (d) TiO_2 NTs in Na_2SO_4+RhB, (e) TiO_2 NTs in Na_2SO_4+MB+RhB, (f) Pd/TiO_2 NTs in Na_2SO_4, (g) Pd/TiO_2 NTs in Na_2SO_4+MB, (h) Pd/TiO_2 NTs in Na_2SO_4+RhB, (i) Pd/TiO_2 NTs in Na_2SO_4+MB+RhB, under illumination.

The electrochemical impedance spectroscopy (EIS) is a powerful tool for studying the interfacial properties between electrodes and solutions. The EIS measurement was carried out covering the frequency of 1 × 10^5 to 0.1 Hz intervals using an amplitude of 10 mV at an open circuit potential. Figure 3a presents Nyquist plots for TiO_2 NTs and Pd/TiO_2 NT-based electrodes in the dark and under illumination. The semicircle at high frequencies is characteristic of the charge transfer process and the diameter of the semicircle is equal to the charge transfer resistance. As depicted, the arch for Pd/TiO_2 NTs is much smaller than that of TiO_2 NTs both in dark and under illumination, indicating that the decoration of Pd nanoparticles significantly enhance the electron mobility by reducing the recombination of electrons and holes. The capacitance measurement on the electrode/electrolyte was conducted at 5k Hz to determine the flat band (U_{FB}) and carrier density (N_D) of TiO_2 NT- and Pd/TiO_2 NT-based electrodes following the equation below[30]

$$\frac{1}{C^2} = \frac{2}{N_D e \varepsilon_0 \varepsilon}\left[(U_S - U_{FB}) - \frac{kT}{e}\right] \qquad (1)$$

where C is the space charge capacitance in the semiconductor; N_D is the electron carrier density; e is the elemental charge value; ε_0 is the permittivity of the vacuum; ε is the relative permittivity of the semiconductor; U_s is the applied potential; T is temperature; and k is the Boltzmann constant. Figure 3b presents the MS plot as $1/C^2$ vs potential. The slopes of the linear parts of the curves in the MS plot are positive, indicating *n*-type semiconductors. The linear parts of the curves are extrapolated to $1/C^2 = 0$, and from eq 1, the values of U_{FB} are estimated to be −0.294 V and −0.137 V for TiO_2 NTs and Pd/TiO_2 NTs, respectively. The positive shift of U_{FB} of Pd/TiO_2 relative to TiO_2 NTs implies a decrease in bending band edge, and thus facilitates the electron transfer. The carrier density N_D can also be determined from Figure 3b, using the following equation[31]

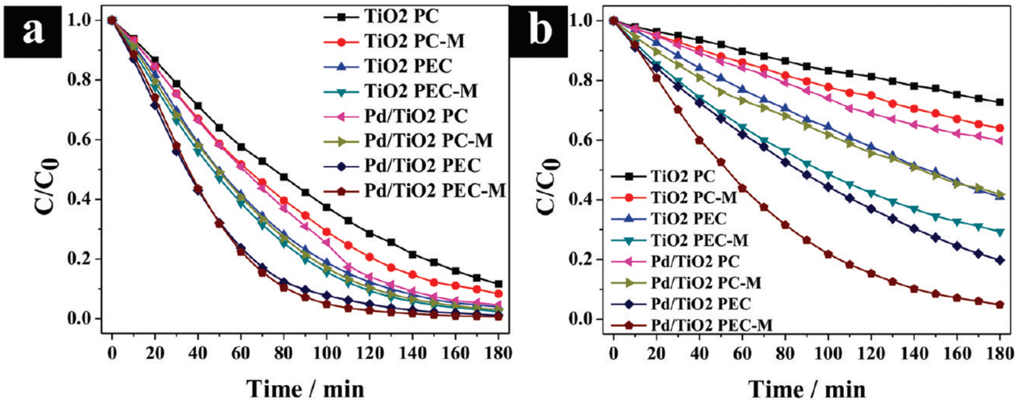

Figure 5. Decomposition of (a) MB and (b) RhB on TiO_2 NTs and Pd/TiO_2 NTs in PC and PEC processes with single and mixed status respectively. (The M in TiO_2 PC-M, TiO_2 PEC-M, Pd/TiO_2 PC-M, Pd/TiO_2 PEC-M denotes mixed dyes conditions.

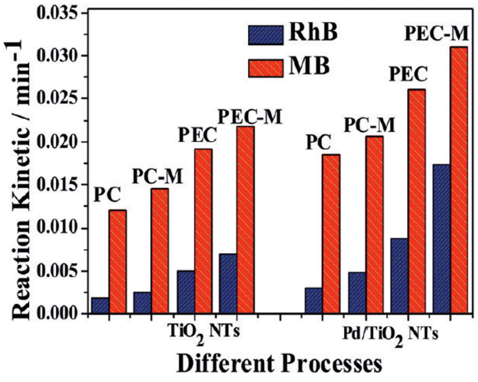

Figure 6. Rate constants (k) on TiO_2 NTs and Pd/TiO_2 NTs in different decomposition processes.

$$N_D = -\left(\frac{2}{e\varepsilon\varepsilon_0}\right)\left(\frac{d(U_s)}{d\left(\frac{1}{C^2}\right)}\right) \tag{2}$$

With $e = 1.6 \times 10^{19}$, $\varepsilon_0 = 8.86 \times 10^{-12}$ F/m, and $\varepsilon = 48$ for anatase TiO_2,[32] the carrier density N_D of TiO_2 NTs and Pd/TiO_2 NTs is calculated to be 2.05×10^{21} and 8.51×10^{22} cm^{-3} respectively. Higher N_D of Pd/TiO_2 NTs implies a faster carrier transfer than TiO_2 NTs and thus a better PC and PEC performance can be expected.

Systematic photoelectrochemical measurements were carried out with TiO_2 NT and Pd/TiO_2 NT electrodes to investigate their activities under various conditions. Figure 4A shows a set of linear sweep voltammagrams (LSV) in dark and under illumination of simulated solar light (AM 1.5, 100 mW/cm^2). In dark, the current on both electrodes was insignificant, with a magnitude of 1×10^{-6} A/cm^2 even at a potential of up to 1.5 V.

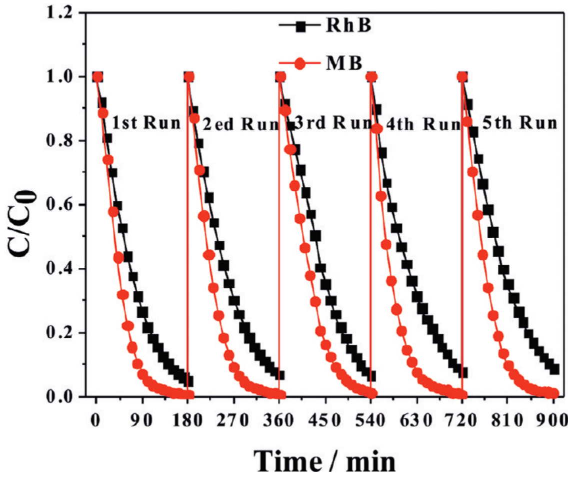

Figure 7. Stability of Pd/TiO_2 NT electrode in PEC processes under illumination of simulated solar light.

Under illumination, a significant increase in the photocurrent was observed on both TiO_2 NT and Pd/TiO_2 NT electrodes. From the LSV data, the following points can be made: (1) the photocurrent density of Pd/TiO_2 NTs was 2 times higher than that on TiO_2 NTs under otherwise same conditions (i.e., no dye, single dye, and mixed dyes), which is in line with the lower charge transfer resistance of Pd/TiO_2 NTs; (2) the existence of the dye(s) increased the photocurrent density on both TiO_2 NTs and Pd/TiO_2 NTs, because the MB and RhB could capture photogenerated holes and thus be decomposed in PEC oxidation processes; (3) in the presence of the mixed dyes, Pd/TiO_2 NTs exhibited a disproportionally high photocurrent density, suggesting a possible synergistic effect between two dyes; (4) in all cases except in dark condition, the photocurrents increased significantly with an increase in the

Table 1. Values of Rate Constant (k), and regression Coefficients (R) of Dye Decomposition in Different Processes on TiO_2 NTs and Pd/TiO_2 NTs

		RhB				MB			
		PC	PC-M	PEC	PEC-M	PC	PC-M	PEC	PEC-M
TiO_2 NTs	k/min^{-1}	0.0018	0.0025	0.005	0.0069	0.003	0.0048	0.0088	0.0173
	R	0.9991	0.9997	0.9982	0.9993	0.9980	0.9993	0.9978	0.9979
Pd/TiO_2 NTs	k/min^{-1}	0.012	0.0145	0.0191	0.0218	0.0185	0.0207	0.0260	0.0310
	R	0.9945	0.9968	0.9978	0.9967	0.9909	0.9968	0.9987	0.9973

Scheme 2. Schematic Illustration of the Energy Bands of Pd/TiO_2 NTs Together with LUMO−HOMO Energy Structures of MB and RhB[a]

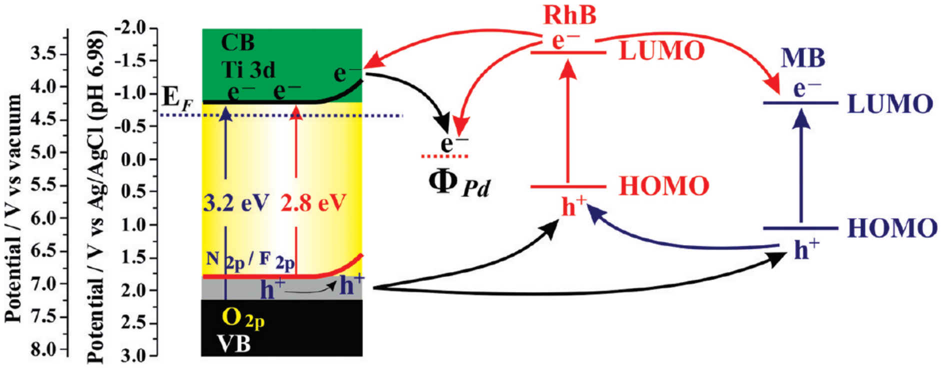

[a] CB, conduction band; VB, valence band; Φ_{Pd}, work function of Pd; e^-, electron; h^+, hole; E_F, Fermi energy level.

applied voltage before it finally leveled off, suggesting that a small external bias is beneficial in driving electron transfer, therefore reducing recombination of photoelectrons and holes from the TiO_2 NTs and Pd/TiO_2 NTs. As recombination of photoelectrons and holes remains a big problem in conventional PC process, an externally applied bias in PEC process clearly works toward solving this problem and thus PEC is advantageous over PC in terms of chemical decomposition. Amperometric *I*−*t* measurements (Figure 4B) recorded fast photoresponses on both TiO_2 NTs and Pd/TiO_2 NTs under conditions of alternating light on and off, and those photocurrent patterns were highly reproducible for many on−off cycles.

Detailed dye decomposition experiments were carried out to evaluate the PC and PEC activities of TiO_2 NT and Pd/TiO_2 NT electrodes. A fixed external bias was selected to be 0.5 V in all PEC processes, as at this potential both TiO_2 NT and Pd/TiO_2 NT electrodes showed saturated photocurrent densities (Figure 4A), and any further increase in the potential beyond this point would not be expected to increase photocurrent. Single MB or RhB, and a mixture of the two dyes, were decomposed in PC and PEC processes separately with 50 mM Na_2SO_4 as a supporting electrolyte under illumination of simulated solar light (AM 1.5, 100 mW/cm^2). The UV−vis absorbance of the MB, RhB, and mixed-dye solutions during PC and PEC processes were recorded periodically to determine their decomposition rates. Panels a and b in Figure 5 present the decomposition kinetics curves of MB and RhB, respectively. First, as expected, the PEC processes are more efficient than PC in degrading the dyes because of the external positive bias driving electrons to reference electrode. Second, in both PC and PEC processes, Pd/TiO_2 NT electrodes showed faster dye decomposition kinetics than TiO_2 NTs, as the Schottky junctions facilitate the electron transfer and thus reduce the recombination of electrons and holes, both contributing to enhanced PEC and PC activities. Furthermore, it is interesting to note that under all conditions, the mixtures of the dyes were decomposed faster than their individual single phase, implying an existence of synergetic effect between the two dyes.

The dye decomposition kinetics data in panels a and b in Figure 5 are found to fit approximately with the first-order kinetic model and the as-fitted values of the rate constant, *k*, are summarized in Figure 6, whereas the numerical values of *k* and regression coefficient, *R*, can be found in Table 1. By comparing the *k* values in Figure 6, the following conclusions can be made: (1) PEC is a more powerful means than PC for the dye decomposition; (2) Pd/TiO_2 NTs are more efficient photocatalysts than TiO_2 NTs, because of the formation of the Schottky junctions; (3) the two dyes when they are mixed show faster decomposition rates for each than when they are in separation, indicating an synergetic effect between the two dyes; (4) the synergetic effect is more remarkable for RhB than for MB decomposition.

Figure 7 presents the stability of Pd/TiO_2 NT electrode during multiple cycles of the mixed dye decomposition in PEC process. Clearly, after five cycles, the Pd/TiO_2 NT electrode did not exhibit any significant loss of their PEC activities, indicating their high stability under operation conditions, which is important for practical applications.

A schematic illustration of the energy bands of the Pd/TiO_2 NTs are depicted in Scheme 2. The doping of N and F reduces the band gap of TiO_2 NTs by increasing the valence band (VB) energy level from O 2p to N 2p or F 2p. Under illumination, the VB electrons of TiO_2 NTs would be excited, and photoelectron−hole pairs are thus generated. Because of the high work function of 5.12 eV of Pd, it facilitates electron transfer from conduction band (CB) of Ti 3d orbital to Pd, which would significantly reduce the recombination of the photogenerated electrons and holes on TiO_2 NTs. The energy level of the lowest unoccupied molecular orbital (LUMO) and the highest occupied molecular orbital (HOMO) of MB are 4.25 and 6.11 eV,[33] respectively, and corresponding LUMO−HOMO energy levels of RhB are 3.50 and 5.60 eV.[34] Supposedly, the observed synergistic effect of the mixed dyes is based on the suitable band alignment of the HUMO-LUMO levels of RhB and MB that match with the band edge positions of Pd/TiO_2 NT. In the mixed-dye system, both RhB and MB can be excited under illumination and the photoelectrons in LUMO of RhB have choices to transfer to lower energy orbits, including Pd, CB of TiO_2, and LUMO of MB. Among them, the electron transfer to CB of TiO_2 would sensitize the TiO_2 NTs, similar to TiO_2 dye-sensitized solar cells systems, and the sensitized TiO_2 NTs would expand their optical absorbance further into the visible-light region, leading to an enhanced PEC activity for decomposition of both RhB and MB. The photogenerated holes on the HOMO of MB can be readily injected into the HOMO of RhB, and therefore the RhB can be degraded by the holes coming from Pd/TiO_2 NTs as well as ones from MB HOMO, which might explain a more significant synergy for RB decomposition than for MB decomposition when the two dyes are together.

4. CONCLUSION

In summary, Pd-nanoparticle-decorated, hierarchical top-porous/bottom-tubular TiO_2 nanostructures were successfully designed and fabricated in facile electrochemical and photochemical processes. The Pd/TiO_2 NTs significantly promoted the electron transfer and thus reduced the recombination of photoelectrons and holes. Compared with the TiO_2 NT electrode, the Pd/TiO_2 NT electrode showed a significant enhancement both on PC and PEC decomposition of organic dyes. Furthermore, a synergy effect between the two mixed dyes was observed during PC and PEC processes, and a mechanism was suggested based on suitable energy level alignment within the system.

■ ASSOCIATED CONTENT

Ⓢ Supporting Information

Additional figures (PDF). This material is available free of charge via the Internet at http://pubs.acs.org.

■ AUTHOR INFORMATION

Corresponding Author

*E-mail: peng.wang@kaust.edu.sa. Tel.: +966-2-8082380.

■ ACKNOWLEDGMENTS

This work was supported by KAUST baseline fund. We thank Dr. Lan Zhao, Dr. Bei Zhang, and Dr. Mohamed Nejib Hedhili from King Abdullah University of Science and Technology (KAUST) for their help with SEM, XRD, and XPS, respectively. Z.Z acknowledges a Sabic Postdoctoral Fellowship.

■ REFERENCES

(1) Chen, X.; Mao, S. S. *Chem. Rev.* **2007**, *107*, 2891−2959.
(2) Zhang, Z. H.; Yuan, Y.; Shi, G. Y.; Fang, Y. J.; Liang, L. H.; Ding, H. C.; Jin, L. T. *Environ. Sci. Technol.* **2007**, *41*, 6259−6263.
(3) In, S.; Nielsen, M. G.; Vesborg, P. C. K.; Hou, Y.; Abrams, B. L.; Henriksen, T. R.; Hansen, O.; Chorkendorff, I. *Chem. Commun.* **2011**, *47*, 2613−2615.
(4) Chen, H.; Chen, S.; Quan, X.; Yu, H.; Zhao, H.; Zhang, Y. *J. Phys. Chem. C* **2008**, *112*, 9285−9290.
(5) Albu, S. P.; Ghicov, A.; Macak, J. M.; Hahn, R.; Schmuki, P. *Nano Lett.* **2007**, *7*, 1286−1289.
(6) Wu, H. J.; Zhang, Z. H. *Int. J. Hydrogen Energy* **2011**, *36*, 13481−13487.
(7) Gong, J.; Lin, C.; Ye, M.; Lai, Y. *Chem. Commun.* **2011**, *47*, 2598−2600.
(8) Zhang, J.; Bang, J. H.; Tang, C.; Kamat, P. V. *ACS Nano* **2010**, *4*, 387−395.
(9) Hamedani, H. A.; Allam, N. K.; Garmestani, H.; El-Sayed, M. A. *J. Phys. Chem. C* **2011**, *115*, 13480−13486.
(10) Das, C.; Roy, P.; Yang, M.; Jha, H.; Schmuki, P. *Nanoscale* **2011**, *3*, 3094−3096.
(11) Varghese, O. K.; Paulose, M.; Grimes, C. A. *Nat. Nanotechnol.* **2009**, *4*, 592−597.
(12) Yan, J.; Zhou, F. *J. Mater. Chem.* **2011**, *21*, 9406−9418.
(13) Park, J. H.; Lee, T. W.; Kang, M. G. *Chem. Commun.* **2008**, 2867−2869.
(14) Yang, M.; Kim, D.; Jha, H.; Lee, K.; Paul, J.; Schmuki, P. *Chem. Commun.* **2011**, *47*, 2032−2034.
(15) Zhang, Z. H.; Hossain, M. F.; Takahashi, T. *Int. J. Hydrogen Energy* **2010**, *35*, 8528−8535.
(16) Ye, M.; Xin, X.; Lin, C.; Lin, Z. *Nano Lett.* **2011**, *11*, 3214−3220.
(17) Wang, F.; Liu, Y.; Dong, W.; Shen, M.; Kang, Z. *J. Phys. Chem. C* **2011**, *115*, 14635−14640.
(18) Ratanatawanate, C.; Tao, Y.; Balkus, K. J. Jr. *J. Phys. Chem. C* **2009**, *113*, 10755−10760.
(19) Wang, L.; Nathan, M. I.; Lim, T. H.; Khan, M. A.; Chen, Q. *Appl. Phys. Lett.* **1996**, *68*, 1267−1269.
(20) Brabec, C. J.; Cravino, A.; Meissner, D.; Sariciftci, N. S.; Fromherz, T.; Rispens, M. T.; Sanchez, L.; Hummelen, J. C. *Adv. Funct. Mater.* **2001**, *11*, 374−380.
(21) Honciuc, A.; Laurin, M.; Albu, S.; Sobota, M.; Schmuki, P.; Libuda, J. *Langmuir* **2010**, *26*, 14014−14023.
(22) Honciuc, A.; Laurin, M.; Albu, S.; Amende, M.; Sobota, M.; Lynch, R.; Schmuki, P.; Libuda, J. *J. Phys. Chem. C* **2010**, *114*, 20146−20154.
(23) Mohapatra, S. K.; Kondamudi, N.; Banerjee, S.; Misra, M. *Langmuir* **2008**, *24*, 11276−11281.
(24) Liu, G.; Li, F.; Wang, D. W.; Tang, D. M.; Liu, C.; Ma, X.; Lu, G. Q.; Cheng, H. M. *Nanotechnology* **2008**, *19*, 025606−026611.
(25) Li, Q.; Shang, J. K. *Environ. Sci. Technol.* **2009**, *43*, 8923−8929.
(26) Yu, J. C.; Zhang, L.; Zheng, Z.; Zhao, J. C. *Chem. Mater.* **2003**, *15*, 2280−2286.
(27) Liu, B.; Zeng, H. C. *Chem. Mater.* **2008**, *20*, 2711−2718.
(28) Fu, Q.; Wagner, T.; Olliges, S.; Carstanjen, H. D. *J. Phys. Chem. B* **2005**, *109*, 944−951.
(29) Wojcieszak, R.; Genet, M. J.; Eloy, P.; Ruiz, P.; Gaigneaux, E. X. *J. Phys. Chem. C* **2010**, *114*, 16677−16684.
(30) Wolcott, A.; Smith, W. A.; Kuykendall, T. R.; Zhao, Y. P.; Zhang, J. Z. *Small* **2009**, *5*, 104−111.
(31) Wang, G.; Wang, Q.; Lu, W.; Li, J. *J. Phys. Chem. B* **2006**, *110*, 22029−22034.
(32) Ghosh, P. K.; Azimi, M. E. *IEEE Trans. Dielectr. Electr. Insul.* **1994**, *1*, 975−981.
(33) Ji, K. H.; Jang, D. M.; Cho, Y. J.; Myung, Y.; Kim, H. S.; Kim, Y.; Park, J. *J. Phys. Chem. C* **2009**, *113*, 19966−19972.
(34) Kato, K.; Takahashi, K.; Suzuki, K.; Sato, T.; Shinbo, K.; Kaneko, F.; Shimizu, H.; Tsuboi, N.; Tadokoro, T.; Ohta, S. *Curr. Appl. Phys.* **2005**, *5*, 321−326.